Optimizing longitudinal spin relaxation in miniaturized optically pumped magnetometers

A.P. McWilliam[1,*] S. Dyer[1] D. Hunter[1] M. Mrozowski[1] S.J. Ingleby[1] O. Sharp[2]
D.P. Burt[2] P.F. Griffin[1] J.P. McGilligan[1] and E. Riis[1]

[1]*Department of Physics, SUPA, University of Strathclyde, Glasgow G4 0NG, United Kingdom*
[2]*Kelvin Nanotechnology, University of Glasgow, Glasgow G12 8LS, United Kingdom*

The microfabrication of cesium vapor cells for optically pumped magnetometry relies on optimization of buffer gas pressure in order to maximize atomic coherence time and sensitivity to external magnetic signals. We demonstrate post-bond nitrogen buffer gas pressure tuning through localized heating of an integrated micropill dispenser. We characterize the variation in the intrinsic longitudinal relaxation rate, γ_{10}, and magnetic sensitivity, as a function of the resulting nitrogen buffer gas pressure. Measurements are conducted by employing an optically pumped magnetometer operating in a free-induction-decay configuration. γ_{10} is extracted across a range of nitrogen pressures between 60 and 700 torr, measuring a minimum of 140 Hz at 115 torr. In addition, we achieve sensitivities as low as 130 fT/$\sqrt{\text{Hz}}$ at a bias field amplitude of about 50 µT. With the optimal nitrogen buffer gas pressure now quantified and achievable post-fabrication, these mass-producible cells can be tailored to suit a variety of sensing applications, ensuring peak magnetometer performance.

I. INTRODUCTION

Precise magnetic field sensing in finite field conditions is crucial in several areas, including geophysical surveying [1], land ordinance [2] and archaeology [3]. In addition, continuous research has revealed promising applications in the medical field, including magnetocardiography and magnetoencephalography [4]. These applications typically require a network of sensors to adequately resolve both spatial and temporal information, and often necessitate gradiometric cancelation when operated in unshielded conditions [5]. Therefore, precise tuning of the buffer gas pressure offers significant advantages by providing consistent sensor performance, improved common-mode noise suppression, and a uniform response across the sensor array.

Optically pumped magnetometers (OPMs) have emerged as a versatile solution for satisfying the numerous sensing requirements across these avenues. OPMs measure the precession frequency of spin-polarized atoms, providing extremely accurate and precise magnetic field readings [6].

Importantly, the incorporation of thermal atomic ensembles in OPMs has enabled miniaturization into portable and chip-scale sensor heads to address real-world implementations [7].

The heart of the OPM comprises an atomic vapor cell, where atom-light interactions occur. Such vapor cells contain the atomic spin medium, in conjunction with a buffer gas or paraffin coating, required to extend the atomic spin-coherence time. A core component in the miniaturization of OPMs is the micromachined vapor cell, typically formed of a glass-silicon-glass stack containing buffer gas to slow the diffusion of the alkali atoms towards the cell walls. Such cells are commonly manufactured with a uniform target buffer gas pressure intended across the entire wafer [8]. Their ability for wafer-scale production enables significantly higher throughput, delivering cost savings compared with commercially available cells created through glass-blowing methods. The reproducibility and achievable yield is of the order of hundreds of cells per wafer, making this approach advantageous for development of sensor arrays and mass-producible quantum technologies [9], with custom geometries and multichamber designs realizable [10–12]. In addition, precise buffer gas control enables the optimization between spatial resolution and sensor precision in OPM magnetic imaging applications [13]. This refinement enables an optimal balance between two factors for peak performance: spin-destruction collisions between alkali and buffer gas atoms, and the atomic diffusion rate.

---

*Contact author: allan.mcwilliam@strath.ac.uk

We employ an OPM based on the free-induction-decay (FID) measurement protocol [14]. One significant advantage of FID-based sensors is their insensitivity to systematics, achieved by temporally separating the optical pumping and detection processes using a pulsed measurement scheme. This separation allows the polarized spins to precess freely at the Larmor frequency without interference from intense pumping light, significantly reducing light shifts and power-broadening effects compared with continuous-wave pumping schemes. In addition, an enhanced optical pumping mode is exploited to facilitate suppression of spin-exchange collisions, reducing the overall spin-relaxation contribution [15]. This vastly extends the sensor's dynamic range to bias fields surpassing the Earth's field (approximately 50 µT).

In this paper we demonstrate the ability to optimize the longitudinal spin-relaxation rate in a micromachined vapor cell by controllable gettering of the nitrogen (N_2) buffer gas pressure from localized heating of an alkali micropill source. The intrinsic spin-relaxation properties for a range of vapor cells are ascertained using the FID approach [13–16]. Power broadening caused by residual optical pumping from the probe light is mitigated through extrapolation to zero-light power [17]. Furthermore, the impact of the buffer gas pressure on the measured sensitivity of the OPM is shown for cell pressures measured between 60 and 700 torr. The ability to optimize the OPM sensitivity and longitudinal relaxation rate by reducing the vapor cell buffer gas pressure in a single vapor cell gives critical insight into the operational characteristics of the sensor. Our findings will guide future mass production of cells with the optimal N_2 pressure content to be applied via backfilling now quantified. Moreover, the N_2 content can be equalized across a population of cells to achieve a uniform response in magnetic gradiometers and OPM sensor arrays.

II. METHODOLOGY

A. Experimental setup

Figure 1(a) displays a simplified schematic of the experimental setup used in this work. We employed three separate vapor cells, which were anodically bonded under different initial N_2 pressure conditions (P_{N_2}). Each cell had dimensions of $(6 \times 6 \times 6)$ mm within the science chamber. Two cells were cylindrically shaped, while the third was characterized by a cuboid geometry. We conducted sequential measurements for each using this OPM setup. The N_2 content was decreased by laser heating the alkali pill source to activate the nonevaporable getter material inside as discussed in [18,19]. P_{N_2} within the cells was determined after each depletion step by performing absorption spectroscopy on the Cs D_1 line with the cell heated to 70°C. The resulting spectrum was then fitted with an absorption profile to extract the N_2 induced pressure broadening and shift, which were used in conjunction with the

coefficients characterized by Andalkar *et al.* [20] to determine the P_{N_2}. The pressure P_{N_2} scales as a function of cell temperature according to the ideal gas law. The cell was operated at 30°C for spin-relaxation measurements to suppress the spin-exchange contributions observed at higher vapor densities, although an appreciable signal could still be observed. The sensitivity was measured at 70°C, which is optimal for the vapor cell configurations considered here. For each measurement throughout this study the cell was placed within a three-layer μ-metal shield to attenuate the Earth's ambient field amplitude and sources of environmental noise.

A set of coils were thermally connected to both sides of the cell using printed circuit boards , as depicted in Fig. 1(a). These coils provided resistive heating and established a well-defined optical pumping (quantization) axis, ensuring high spin polarization even in the presence of substantial bias fields. This is due to the strong magnetic field, $|\vec{B}_{Pol}| > 1$ mT, applied along the quantization axis by the coils, which greatly exceeds the fields within the measurement range of interest [15]. Surrounding the cell were a set of Helmholtz coils which provided static transverse magnetic field control. This coil set was driven by a programmable low-noise current driver that does not contribute significantly to the overall noise budget of the sensor [21].

We operated a two-color pump-probe scheme as described in previous works [13,15]. Strong pulsed optical pumping was applied (approximately 120 mW peak power) with circularly polarized light on the pressure-broadened $F = 3 \rightarrow F'$ hyperfine transition of the Cs D_2 line. The pump light was extinguished from peak optical power to <5 µW using an acousto-optic modulator . The pump light recycles atomic population present in the $F = 3$ manifold which is subsequently redistributed to the $F = 4$ ground state, inducing an orientation in the atomic ensemble. This is akin to the hyperfine-repump technique employed in [22], albeit without an additional laser source. Moreover, the continuous absorption and emission process transfers a large net spin polarization into a stretched Zeeman state with maximum angular momentum $m_F = 4$. Collision of atoms occupying the same hyperfine ground state does not result in decoherence through spin exchange, therefore efficient optical pumping to a highly stretched state allows effective suppression of spin-exchange dephasing [23].

Detection was performed on the Cs D_1 line with a weaker probe beam, less than 1.2% of the pump beam's peak optical power. The probe frequency was set approximately 21 GHz blue-detuned from the $F = 3 \rightarrow F'$ transition. This was close enough to resonance to yield an appreciable signal amplitude, while avoiding excessive power broadening due to residual optical pumping. To obtain the intrinsic spin-relaxation property, γ_{10}, it was necessary to negate these operational systematics further.
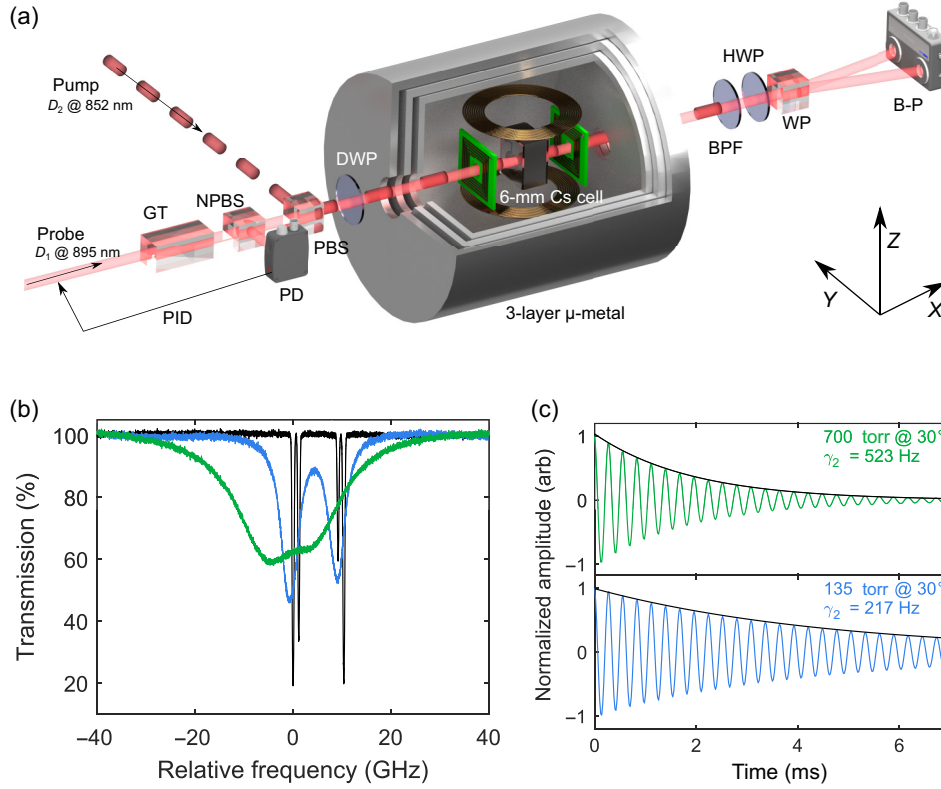
FIG. 1. (a) OPM experimental setup containing 852-nm and 895-nm pump and probe beams that interact with cesium (Cs) atoms in a thermal vapor cell placed in a magnetic shield with a controlled bias field applied along the z axis. The transmitted probe was detected with a balanced polarimeter while the residual pump was blocked with a spectral filter. GT, Glan-Thompson polarizer; NPBS, nonpolarizing beamsplitter; PBS, polarizing beamsplitter; DWP, dual-wavelength waveplate; BPF, band-pass filter; WP, Wollaston prism; B-P, balanced polarimeter; PD, photodiode used in conjunction with an acousto-optic modulator (not pictured) for probe beam intensity stabilization. (b) Absorption spectroscopy (Cs D_1 line) was used to extract (N$_2$) pressure readings with spectra shown for 700 torr (green) and 135 torr (blue) compared with a Cs reference cell (black). (c) Corresponding FID signal data relating to a probe power of 1.3 mW along with relaxation envelopes (black). The probe beam induces a broadening effect, γ_P, leading to an increase in the relaxation rate.

This was achieved by applying a range of probe powers from about 0.1 mW to 1.3 mW such that γ_{10} could be ascertained by extrapolating to zero-light power. The probe power was measured before transmission through the cell, which was at least 70%. The pump and probe beams were ensured to overlap at the center of the cell, where they both possessed a 3.1 mm beam diameter ($1/e^2$). Therefore, both were sufficiently well contained inside the cell volume to avoid beam clipping.

B. Signal analysis

A balanced polarimeter (Thorlabs PDB210A), which rejects common-mode laser intensity noise, was used to capture the signal. A data acquisition device (Picoscope Model 5444D) sampled at a base rate of $f_s = 125$ MHz and functioned with 15-bit voltage resolution. Oversampling was performed to average 25 successive data points, resulting in a decimated sample rate of $f_s = 1/\Delta t = 5$ MHz. This was due to f_s greatly exceeding the signals of

interest, which oscillated at either 3.5 kHz (Sec. III A) or 175 kHz (Sec. III B). Furthermore, for the former in post-process a low-pass Butterworth filter (second order) was applied to suppress any spurious higher-frequency noise. This data was also further down-sampled by a factor of 100 to reduce the effective sample rate to $f_s = 50$ kHz (equating to approximately 14 points per cycle). This served only to expedite the fitting analysis and did not corrupt the extracted fit parameters.

The FID signal manifests as a result of optical rotation of the probe beam polarization, which maps the induced spin-polarization precessing around the magnetic field at the Larmor frequency. The digitized FID signal can be represented as follows:

$$S_n = A \sin(\omega_L n \Delta t + \phi_0)\, e^{-\gamma_2 n \Delta t} + \epsilon_n. \tag{1}$$

where A is the signal amplitude, relating to the spin polarization generated during the optical pumping phase, ω_L

is the Larmor precession frequency, and ϕ_0 is the initial phase. Here n relates to the sample data point under consideration and ϵ_n represents noise present in the signal. Nonlinear fitting was applied with the Levenberg-Marquardt algorithm [24] using a damped sinusoidal model to extract the relevant parameters. After optical pumping, the precessing atomic spin polarization decays as the polarization returns to its equilibrium (unpolarized) state, with a total spin-relaxation rate denoted by γ_2. Section II C describes methods of lowering γ_2 such that this equates to the intrinsic longitudinal rate of the vapor cell. This was enabled by reducing the cell temperature and probe power with the results presented in Sec. III A. In Sec. III B our chosen operating regime involved the vapor density being raised to increase atom-light interactions, thus elevating γ_2. However, this ultimately enhanced the sensitivity and provided a better analog for a practical sensor with optimized performance.

C. Relaxation rate measurements

The spin-relaxation rate limits the total possible measurement time of the OPM. The various intrinsic relaxation mechanisms inherent in vapor cells are extensively described in [25]. The intrinsic longitudinal relaxation rate, γ_{10}, is the ultimate spin-relaxation limit. The main contributions to this in this study arise from alkali-wall collisions (γ_{WC}) and alkali-buffer gas collisions (γ_{BG}). A negligible contribution to the spin decoherence arises through Cs-Cs spin-destruction collisions (γ_{SD}). The cross section for this is a factor of about 100 smaller than Cs-Cs spin-exchange collisions [26,27]. Therefore, γ_{10} is defined as

$$\gamma_{10} = \gamma_{WC} + \gamma_{BG} + \gamma_{SD}. \quad (2)$$

The aggregated term representing the total transverse relaxation rate, γ_2, including operational systematics, is given by

$$\gamma_2 = \gamma_{10} + \gamma_{SE} + \gamma_P + \gamma_{\Delta B}. \quad (3)$$

Therefore, to successfully extract the intrinsic relaxation rate, γ_{10}, the additional relaxation contributions including optical power broadening (γ_P), magnetic gradients across the cell ($\gamma_{\Delta B}$), and spin-exchange collisions (γ_{SE}) have to be suppressed.

Operating the system at a low bias magnetic field strength of $|\vec{B}_z| \approx 1\ \mu T$ lowered magnetic gradients to $\gamma_{\Delta B} < 1$ Hz based on calculations considering the coil geometry and vapor cell dimensions. Furthermore, spin-exchange collisions are negligible at the low cell temperatures ($T = 30°C$) considered here. Temperature was monitored using three nonmagnetic T-type thermocouple sensors attached to separate positions of the cell. All agreed to within $0.1\,°C$, confirming a uniform temperature across the cell. The cell was not found to drift by more
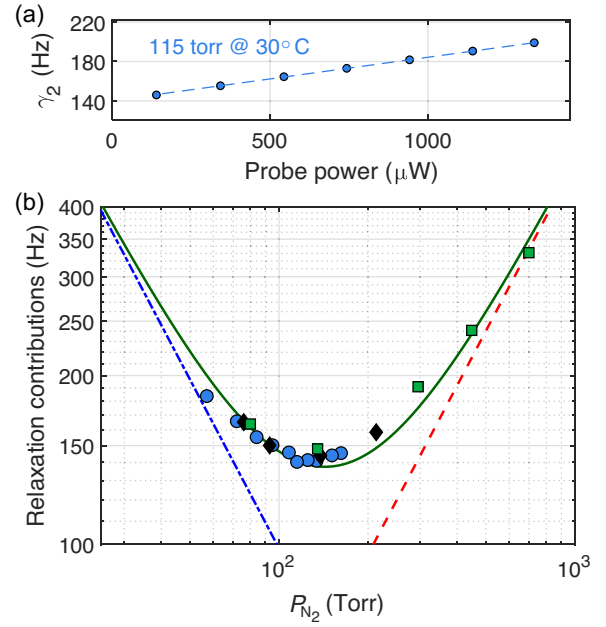

FIG. 2. (a) Measured values for γ_2 as a function of probe power for $P_{N_2} = 115$ torr, where γ_{10} is minimized. Extrapolation to zero-light power at each N_2 pressure provides the respective γ_{10} values shown in (b). The spin exchange and magnetic field broadening contributions to γ_2 were minimal throughout these spin-relaxation measurements. (b) Blue data points relate to measurements with the cuboid cell. Black and green data points refer to two separate cylindrical shaped cells. The various lines relate to the theoretical spin-relaxation mechanisms: γ_{10} (green solid line); γ_{WC} (blue dot-dashed line); γ_{BG} (red dashed line). Error bars are smaller than the markers.

than $0.1\,°C$ over the course of each set of measurements. It should be noted that an insignificant increase in γ_{10} occurs for increasing temperatures.

The pump-probe cycle was applied at a repetition rate, R_r, of 10 Hz with a pump duration, T_{OP}, of 5 ms and total probing duration, T_{PR}, of 95 ms. This measurement period ensured the atoms fully decohered and rethermalized before subsequent optical pumping cycles occurred, thus avoiding fitting systematics from signal truncation. To determine the intrinsic relaxation rate under these conditions, measurements were taken at various probe powers, starting from a maximum of 1.3 mW and decreasing incrementally to 140 μW. Nonlinear fitting using a damped sinusoidal model [Eq. (1)] was applied to the FID datasets to extract γ_2 in each case. A linear extrapolation to zero-light power accounts for the contribution from γ_P such that γ_{10} can be determined as seen in Fig. 2(a).

III. RESULTS

A. Relaxation rate results

Figure 2(b) displays the results over the full buffer gas pressure range. Each pressure iteration produced small

statistical errors for each data point of the order of 1 Hz. The data demonstrate a continuous optimization of γ_{10} when lowering P_{N_2} to 115 torr, which is where it is minimized. Then γ_{10} begins to increase as P_{N_2} is reduced further due to Cs-wall collisions (γ_{WC}) becoming the dominant depolarizing mechanism and the contribution from Cs-N_2 collisions (γ_{BG}) diminishing. Across the pressure range $P_{N_2} \approx 57$–212 torr, the intrinsic relaxation rate ranges over $\gamma_{10} \approx 140$–184 Hz. This equates to intrinsic spin-coherence times of between 5.4 ms and 7.1 ms. Moreover, γ_{10} maintains a consistency below 150 Hz between a range of 108–162 torr, showcasing a fairly wide pressure range that permits extensive coherence times. This is a significant time period in which magnetic sensing measurements can be made before spin relaxation occurs, providing enhanced sensitivity performance.

The data align with the theoretical model outlined in [25] when constraining all known parameters, with the exception of two critical parameters: the Cs-N_2 spin-destruction rate, σ_{Cs-N_2}; and the Cs diffusion coefficient in N_2, $D_{0:Cs-N_2}$. The data indicates that these values are $\sigma_{Cs-N_2} = 2.9 \times 10^{-26}$ m^2 and $D_{0:Cs-N_2} = 0.12$ cm^2 s^{-1} respectively. This value for $D_{0:Cs-N_2}$ matches well with the works from [28–31] which have published values for each. σ_{Cs-N_2} resides within a fairly wide spectrum of these published results. More recent data for these parameters are not readily available. The disparity of measured values from the literature makes it reasonable to incorporate these values in the model as they concur with the observed data. This alignment is further supported by the reliability of our measurements, involving multiple data points with three distinct cells which agree for similar P_{N_2} values.

Previously, we have demonstrated that our heating and enhanced optical pumping strategy does not cause additional systematics to γ_{10} by perturbing the precessing ensemble [15]. This was further verified in this work by collecting data at room temperature ($T \approx 21\,^\circ$C), without current being applied through the resistive heating coils. We obtained a value of $\gamma_{10} \approx 139$ Hz at $P_{N_2} \approx 125$ torr, which is 2 Hz lower than the 141 Hz extracted when the cell was heated to $30\,^\circ$C. This agrees with theoretical predictions for $\Delta\gamma_{10}$ for this temperature variation.

B. Sensitivity results

Assessment of the achievable sensitivity performance of the sensor required raising of the vapor density. Therefore, the cell was heated to $70\,^\circ$C for each P_{N_2} iteration. This elevated temperature results in an increase in the rate of spin-exchange collisions. Demonstrating the system's candidacy for unshielded applications also required increasing the bias field to $|\vec{B}_z| \approx 50\,\mu$T. To minimize technical magnetic noise contributions (e.g., power line noise), the current through the Helmholtz coils was driven by connecting a 12-V battery to a resistor in series. Consistent pump and
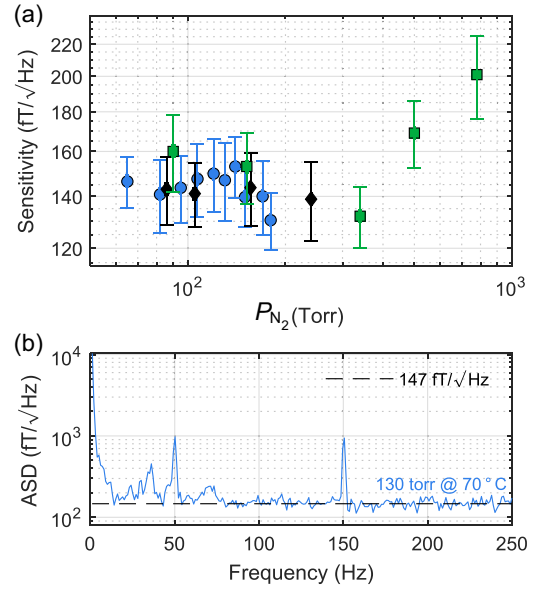

FIG. 3. (a) OPM sensitivity measured across a range of N_2 pressures at $|\vec{B}_z| \sim 50\,\mu$T bias field. The error bars were calculated from the standard deviation in the noise densities from each associated amplitude spectral density (ASD) over a 70–250-Hz frequency range, excluding technical noise peaks. Negligible change occurs between $P_{N_2} \approx 57$ and 340 torr, providing an extensive buffer gas target range to aim for in future fabrication for optimal sensitivity performance. (b) ASD at $P_{N_2} \approx 130$ torr, $T \approx 70\,^\circ$C, and a probe power of 1.2 mW. A sensitivity of 147 ± 11 fT/$\sqrt{\text{Hz}}$ was calculated.

probe powers of 120 mW and 1.2 mW were respectively employed throughout. Here R_r, was set to 500 Hz with an optical pumping duty cycle of 10%, equating to $T_{OP} = 0.2$ ms and $T_{PR} = 1.8$ ms for each FID cycle. A faster R_r here aids the sensitivity performance, which can be optimized based on the decoherence rate and the Cramér-Rao lower bound (CRLB) condition [32,33]. In contrast to Sec. III A, subsequent optical pumping cycles were commenced before the atoms fully decohered or rethermalized to maximize sensor bandwidth and sensitivity.

Each evaluation of the magnetic sensitivity involved capturing a sequence of FID signal trains. Forty independent FID trains were recorded over time periods of 1 s and subsequently processed to provide a time series of the magnetic field magnitude. The corresponding amplitude spectral densities (ASDs) were averaged using Welch's method to provide a smoother spectrum [34]. Figure 3(a) displays the sensitivity results across the full buffer gas range for each cell. An example of the ASD for $P_{N_2} = 130$ torr is displayed in (b).

The experimental sensitivities improved as P_{N_2} was reduced from 780 to 340 torr. Between 57 and 340 torr a consistent performance was found with measured experimental sensitivities between 130 and 160 fT/$\sqrt{\text{Hz}}$. The best sensitivity of 130 ± 11 fT/$\sqrt{\text{Hz}}$ was found to occur at a buffer gas pressure of 180 torr. Notably, line and technical

noise peaks are observable, indicating coupling through the electronics and magnetic environment. Variations in the amplitude and frequencies of these peaks are also evident.

These results equate to around 3 parts per billion in fractional sensitivity terms [35], representing a state-of-the-art resolution using a micromachined vapor cell. These results owe much to the manufacturing, with the 6-mm thickness reducing the relaxation rates while also improving the signal amplitude in comparison with our previous works with 3-mm- thick cells [13,15]. In addition, the intense pump light combined with applying $\vec{B}_{Pol}$ greatly assists in maintaining the spin polarization during the atomic state preparation. Micromachined cells have previously shown higher sensitivities than the work here; however, this was at a lower magnetic field amplitude [36]. In that work, magnetic field nulling was used during the optical pumping stage, ultimately producing a sensitivity of around $100 \text{ fT}/\sqrt{\text{Hz}}$. While demonstrating excellent sensitivity, the advantage of our approach is that it circumvents the need for measuring the field and subsequently nulling it. This presents an advantage for unshielded sensing as it reduces dead time and bypasses potential issues incurred in dynamic magnetic environments (e.g., sensing on board moving vehicles or vessels).

IV. CONCLUSION

Our micromachining capabilities have led to successful production of vapor cells with 6-mm optical path lengths (single pass). Extensive measurements were made to extract the intrinsic longitudinal spin-relaxation rate, γ_{10}, which sets the ultimate limit on spin relaxation, across a range of buffer gas pressures using three distinct vapor cells. We have demonstrated a successful application of buffer gas pressure tuning to reach the optimal value where γ_{10} is minimized. A minimum of 140 Hz was found, measured at a cell temperature of $30\,^\circ\text{C}$ and $P_{N_2} = 115$ torr. Further reduction of γ_{10} will be challenging without further increasing the cell size or thickness.

Pivoting to fabrication approaches which do not include a buffer gas would circumvent these spin-destructive alkali-buffer gas collisions; however, the antirelaxation coatings required to preserve spin coherence are not compatible with the temperatures required for anodic bonding. In addition, the optical pumping efficiency which is enhanced through the use of a quenching gas agent would be lost. Overall, our results indicate that the differing geometry of cells does not markedly impact the cell performance characteristics. This is an encouraging result which bodes well for mass cell fabrication as this indicates a level of consistency. A noteworthy finding is the large buffer gas pressure range at which prolonged relaxation times are achieved.

We have demonstrated sensitivities reaching state-of-the-art levels for microfabricated vapor cells in bias fields emulating Earth's field conditions (approximately $50\,\mu\text{T}$). We obtained a minimum of $130 \pm 11 \text{ fT}/\sqrt{\text{Hz}}$. Clearly sensitivities at these levels in geophysical fields are of value in several finite-field OPM applications. In addition, our results validate the fabrication and activation approach employed for these cells. This study has demonstrated the large buffer gas pressure range at which exemplary sensor performance is attainable. One of the main advantages of the buffer gas tuning approach is the ability to decrease the pressure post fabrication. Recent studies have demonstrated technical capabilities to sequentially increase the buffer gas pressure within microfabricated cells via a break-seal technique that well complements the methods demonstrated in this work [37]. Magnetic gradiometers would undoubtedly benefit from this, as the capacity to finely adjust the pressure to achieve uniformity across identical cell geometries is desirable [38,39].

The data that support the findings of this study are available from the corresponding author upon reasonable request.

[1] M. Nabighian, M. Ander, V. Grauch, R. Hansen, T. Lafehr, Y. Li, W. Pearson, J. Peirce, J. Phillips, and M. Ruder, 75th anniversary—Historical development of the gravity method in exploration, Geophysics **70**, 63ND (2005).

[2] S. Billings, C. Pasion, S. Walker, and L. Beran, Magnetic models of unexploded ordnance, IEEE Trans. Geosci. Remote Sens. **44**, 2115 (2006).

[3] H. Becker, From nanotesla to picotesla—A new window for magnetic prospecting in archaeology, Archaeol. Prospect. **2**, 217 (1995).

[4] M. Limes, E. Foley, T. Kornack, S. Caliga, S. McBride, A. Braun, W. Lee, V. Lucivero, and M. Romalis, Portable magnetometry for detection of biomagnetism in ambient environments, Phys. Rev. Appl. **14**, 011002 (2020).

[5] R. Zhang, W. Xiao, Y. Ding, Y. Feng, X. Peng, L. Shen, C. Sun, T. Wu, Y. Wu, Y. Yang, Z. Zheng, X. Zhang, J. Chen, and H. Guo, Recording brain activities in unshielded earth's field with optically pumped atomic magnetometers, Sci. Adv. **6**, eaba8792 (2020).

[6] D. Budker and M. Romalis, Optical magnetometry, Nat. Phys. **3**, 227 (2006).

[7] S. Ingleby, P. Griffin, T. Dyer, M. Mrozowski, and E. Riis, A digital alkali spin maser, Sci. Rep. **12**, 1 (2022).

[8] J. P. McGilligan, K. Gallacher, P. F. Griffin, D. J. Paul, A. S. Arnold, and E. Riis, Micro-fabricated components for cold atom sensors, Rev. Sci. Instrum. **93**, 091101 (2022).

[9] Y. Li, D. B. Sohn, M. Hummon, and J. Kitching, Wafer level fabrication of evacuated alkali vapor cells, Opt. Lett. **49,** 4963–4966 (2024).

[10] S. Dyer, P. F. Griffin, A. S. Arnold, F. Mirando, D. P. Burt, E. Riis, and J. P. McGilligan, Micro-machined deep silicon atomic vapor cells, J. Appl. Phys. **132,** 134401 (2022).

[11] H. Raghavan, M. C. D. Tayler, K. Mouloudakis, R. Rae, S. Lähteenmäki, R. Zetter, P. Laine, J. Haesler, L. Balet, T. Overstolz, S. Karlen, and M. W. Mitchell, Functionalized mm-scale vapor cells for alkali-metal spectroscopy and magnetometry, Phys. Rev. Appl. **22,** 044011 (2024).

[12] J. Kitching, Chip-scale atomic devices, Appl. Phys. Rev. **5,** 031302 (2018).

[13] D. Hunter, C. Perrella, A. McWilliam, J. P. McGilligan, M. Mrozowski, S. J. Ingleby, P. F. Griffin, D. Burt, A. N. Luiten, and E. Riis, Free-induction-decay magnetic field imaging with a microfabricated Cs vapor cell, Opt. Express **31,** 33582 (2023).

[14] D. Hunter, S. Piccolomo, J. D. Pritchard, N. L. Brockie, T. E. Dyer, and E. Riis, Free-induction-decay magnetometer based on a microfabricated Cs vapor cell, Phys. Rev. Appl. **10,** 014002 (2018).

[15] D. Hunter, M. S. Mrozowski, A. McWilliam, S. J. Ingleby, T. E. Dyer, P. F. Griffin, and E. Riis, Optical pumping enhancement of a free-induction-decay magnetometer, J. Opt. Soc. Am. B **40,** 2664 (2023).

[16] D. Hunter, R. Jiménez-Martínez, J. Herbsommer, S. Ramaswamy, W. Li, and E. Riis, Waveform reconstruction with a Cs based free-induction-decay magnetometer, Opt. Express **26,** 30523 (2018).

[17] T. Scholtes, S. Woetzel, R. IJsselsteijn, V. Schultze, and H.-G. Meyer, Intrinsic relaxation rates of polarized Cs vapor in miniaturized cells, Appl. Phys. B **117,** 211 (2014).

[18] S. Dyer, A. McWilliam, D. Hunter, S. Ingleby, D. P. Burt, O. Sharp, F. Mirando, P. F. Griffin, E. Riis, and J. P. McGilligan, Nitrogen buffer gas pressure tuning in a micro-machined vapor cell, Appl. Phys. Lett. **123,** 074001 (2023).

[19] V. G. Lucivero, A. Zanoni, G. Corrielli, R. Osellame, and M. W. Mitchell, Laser-written vapor cells for chip-scale atomic sensing and spectroscopy, Opt. Express **30,** 27149 (2022).

[20] A. Andalkar and R. B. Warrington, High-resolution measurement of the pressure broadening and shift of the Cs D_1 and D_2 lines by N_2 and He buffer gases, Phys. Rev. Appl. **65,** 7 (2002).

[21] M. S. Mrozowski, I. C. Chalmers, S. J. Ingleby, P. F. Griffin, and E. Riis, Ultra-low noise, bi-polar, programmable current sources, Rev. Sci. Instrum. **94,** 014701 (2023).

[22] V. Schultze, T. Scholtes, R. IJsselsteijn, and H.-G. Meyer, Improving the sensitivity of optically pumped magnetometers by hyperfine repumping, J. Opt. Soc. Am. B **32,** 730 (2015).

[23] T. Scholtes, V. Schultze, R. IJsselsteijn, S. Woetzel, and H.-G. Meyer, Light-narrowed optically pumped M_x magnetometer with a miniaturized Cs cell, Phys. Rev. Appl. **84,** 043416 (2011).

[24] I. Hughes and T. Hase, *Measurements and Their Uncertainties: A Practical Guide to Modern Error Analysis* (Oxford University Press (OUP), Oxford, 2010).

[25] T. Scholtes, S. Woetzel, R. IJsselsteijn, V. Schultze, and H.-G. Meyer, Intrinsic relaxation rates of polarized Cs vapor in miniaturized cells, Appl. Phys. B **117,** 211 (2014).

[26] N. W. Ressler, R. H. Sands, and T. E. Stark, Measurement of spin-exchange cross sections for ^{133}Cs, ^{87}Rb, ^{85}Rb, ^{39}K, and ^{23}Na, Phys. Rev. **184,** 102 (1969).

[27] T. G. Walker and W. Happer, Spin-exchange optical pumping of noble-gas nuclei, Rev. Mod. Phys. **69,** 629 (1997).

[28] F. A. Franz and E. Lüscher, Spin relaxation of optically pumped cesium, Phys. Rev. **135,** A582 (1964).

[29] N. Beverini, P. Minguzzi, and F. Strumia, Foreign-gas-induced cesium hyperfine relaxation, Phys. Rev. Appl. **4,** 550 (1971).

[30] F. A. Franz and C. E. Sooriamoorthi, Spin relaxation within the $6^2p_{\frac{1}{2}}$ and $6^2s_{\frac{1}{2}}$ states of cesium measured by white-light optical pumping, Phys. Rev. Appl. **10,** 126 (1974).

[31] J. Kitching, S. Knappe, and L. Hollberg, Miniature vapor-cell atomic-frequency references, Appl. Phys. Lett. **81,** 553 (2002).

[32] C. Gemmel, W. Heil, S. Karpuk, K. Lenz, C. Ludwig, Y. Sobolev, K. Tullney, M. Burghoff, W. Kilian, S. Knappe-Grüneberg, W. Müller, A. Schnabel, F. Seifert, L. Trahms, and S. Baeßler, Ultra-sensitive magnetometry based on free precession of nuclear spins, Eur. Phys. J. D **57,** 303 (2010).

[33] A. Jaufenthaler, T. Kornack, V. Lebedev, M. Limes, R. Körber, M. Liebl, and D. Baumgarten, Pulsed optically pumped magnetometers: Addressing dead time and bandwidth for the unshielded magnetorelaxometry of magnetic nanoparticles, Sensors **21,** 1212 (2021).

[34] P. Welch, The use of fast fourier transform for the estimation of power spectra: A method based on time averaging over short, modified periodograms, IEEE Trans. Audio Electroacoustics **15,** 70 (1967).

[35] N. Wilson, P. Light, A. Luiten, and C. Perrella, Ultrastable optical magnetometry, Phys. Rev. Appl. **11,** 044034 (2019).

[36] V. Gerginov, M. Pomponio, and S. Knappe, Scalar magnetometry below 100 fT/Hz$^{1/2}$ in a microfabricated cell, IEEE Sens. J. **20,** 12684 (2020).

[37] V. Maurice, C. Carlé, S. Keshavarzi, R. Chutani, S. Queste, L. Gauthier-Manuel, J.-M. Cote, R. Vicarini, M. Abdel Hafiz, R. Boudot, and N. Passilly, Wafer-level vapor cells filled with laser-actuated hermetic seals for integrated atomic devices, Microsyst. Nanoeng. **8,** 129 (2022).

[38] R. Zhang, R. Mhaskar, K. Smith, and M. Prouty, Portable intrinsic gradiometer for ultra-sensitive detection of magnetic gradient in unshielded environment, Appl. Phys. Lett. **116,** 143501 (2020).

[39] D. Sheng, A. R. Perry, S. P. Krzyzewski, S. Geller, J. Kitching, and S. Knappe, A microfabricated optically-pumped magnetic gradiometer, Appl. Phys. Lett. **110,** 031106 (2017).